Observation of topological transition in high-T_c superconducting monolayer $FeTe_{1-x}Se_x$ films on $SrTiO_3(001)$

X.-L. Peng,[1,2] Y. Li,[1,2] X.-X. Wu,[3] H.-B. Deng,[1,2] X. Shi,[1,2] W.-H. Fan,[1,2] M. Li,[4] Y.-B. Huang,[4] T. Qian,[1,5,6] P. Richard,[7] J.-P. Hu,[1,2,5,6] S.-H. Pan,[1,2,5,6] H.-Q. Mao,[1,*] Y.-J. Sun,[1,5,6,†] and H. Ding[1,2,5,6,‡]

[1]*Beijing National Laboratory for Condensed Matter Physics, and Institute of Physics, Chinese Academy of Sciences, Beijing 100190, China*

[2]*School of Physics, University of Chinese Academy of Sciences, Beijing 100190, China*

[3]*Institut für Theoretische Physik und Astrophysik, Julius-Maximilians-Universität Würzburg, Würzburg 97074, Germany*

[4]*Shanghai Synchrotron Radiation Facility, Shanghai Institute of Applied Physics, Chinese Academy of Sciences, Shanghai 201204, China*

[5]*Songshan Lake Materials Laboratory, Dongguan, Guangdong 523808, China*

[6]*CAS Center for Excellence in Topological Quantum Computation, University of Chinese Academy of Sciences, Beijing 100190, China*

[7]*Institut quantique, Université de Sherbrooke, 2500 boulevard de l'Université, Sherbrooke, Québec, Canada J1K 2R1*

(Received 14 March 2019; revised manuscript received 1 October 2019; published 21 October 2019)

Superconductors with topological surface or edge states have been intensively explored for the prospect of realizing Majorana bound states, which obey non-Abelian statistics and are crucial for topological quantum computation. The traditional routes for making topological insulator/superconductor and semiconductor/superconductor heterostructures suffer fabrication difficulties and can only work at low temperature. Here, we use angle-resolved photoemission spectroscopy to directly observe the evolution of a topological transition of band structure nearby the Fermi level in two-dimensional high-T_c superconductor $FeTe_{1-x}Se_x/SrTiO_3(001)$ monolayers, fully consistent with our theoretical calculations. Furthermore, evidence of edge states is revealed by scanning tunneling spectroscopy with assistance of theoretical calculations. Our study provides a simple and tunable platform for realizing and manipulating Majorana states at high temperature.

DOI: 10.1103/PhysRevB.100.155134

I. INTRODUCTION

Topological superconductors, which can host Majorana bound states on their surface or edge, have drawn enormous attention in condensed matter physics [1,2]. This is because the non-Abelian braiding properties of Majorana states are predicted to play an essential role in topological quantum computation. Intrinsic p-wave superconductors [3,4] and heterostructures of s-wave superconductors and topological insulators/Rashba-type semiconductors [5,6] are two typical routes for realizing topological superconductors (or more precisely, superconducting topological states). However, the former suffers from the scarcity of candidate materials and their sensitivity to disorder, whereas the latter suffers from structural complexities and low working temperatures, hindering manipulation of Majorana states in applications. Recently, bulk superconductors with topological surface states [7–15] provide a new route, where ordinary superconductivity and nontrivial topology can be integrated in a single material, such as $FeTe_{0.55}Se_{0.45}$ [8–11], Bi_2Pd [12], and other iron-based superconductors [13–15]. Among them, the most interesting systems are the high-T_c superconductors, which can significantly raise the working temperature.

Monolayer FeSe grown on $SrTiO_3(001)$ (STO) holds the highest T_c (above 65 K [16–23]) among all iron-based superconductors and can potentially combine superconductivity and topological properties into a single material [24–26]. One way of integration is to adjust lattice parameters, for example by substituting selenium by tellurium, which maintains high T_c for monolayer $FeTe_{1-x}Se_x$ films within a wide range of substitution, as revealed by previous scanning tunneling microscopy/spectroscopy (STM/STS) [27] and angle-resolved photoemission spectroscopy (ARPES) results [28]. Moreover, a theoretical work predicted that the monolayer $FeTe_{1-x}Se_x$ system can realize topological nontrivial states through band inversion at the Γ point [29] and some supporting evidence was found later in ARPES measurements [28]. However, the topological nontrivial characters of the monolayer system have not been determined yet, which hinders their applications as a simple and tunable platform for realizing topological superconductivity at high temperature.

In this paper, we perform systematic ARPES measurements with photon energy and polarization dependence on $FeTe_{1-x}Se_x$/STO monolayers with different Se content (x) grown by *in situ* molecular beam epitaxy (MBE). The direct observation of orbital character and parity changes with decreasing Se content (x) provides convincing evidence to the occurrence of topological transition in these systems. In addition to the observation of electronlike and holelike bands intersecting at the Γ point, the striking change of the effective mass of bands with p_z and d_{xz} orbital characters around the topological critical point ($x = 0.21$) further supporting it. The

*mhq@iphy.ac.cn
†yjsun@iphy.ac.cn
‡dingh@iphy.ac.cn

appearance of electronlike band with p_z orbital at the Γ point indicates that the topological transition is driven by the anion height which tunes the hybridization between chalcogenide anions and iron cations. Furthermore, evidence of edge states of monolayer FeTe/STO is observed by STM/STS measurements in combination with theoretical calculations, consisting of a plateau in density of states (DOS) for one-dimensional (1D) Dirac cone around 20 meV below the Fermi level (E_F) and the enhancement of DOS around 50 meV below E_F.

II. EXPERIMENTAL AND COMPUTATIONAL METHODS

Monolayer $FeTe_{1-x}Se_x$ for *in situ* ARPES measurements are grown on 0.7 wt % Nb-doped STO substrates after degassing for 10 h at 600 °C and then annealing for 1.5 h at 950 °C in an ultrahigh-vacuum MBE chamber. Substrates are kept at 310 °C for monolayer FeSe and 275 °C for monolayer $FeTe_{1-x}Se_x$ during the film growth. Fe (99.98%), Se (99.999%), and Te (99.99%) are coevaporated from Knudsen cells. The flux ratio of Fe to Se/Te is 1:10, which is measured by a quartz crystal balance. The growth rate is determined by Fe flux and equals 0.7 UC/min. The Se content (x) is controlled by the ratio of Te to Se flux speed during growth. After growth, the monolayer FeSe films are annealed at 370 °C and monolayer $FeTe_{1-x}Se_x$ at 260 °C for 20 h. Then, the samples are transferred *in situ* to the ARPES chamber for measurements. ARPES measurements are recorded at the BL-09U "Dreamline" beamline of Shanghai Synchrotron Radiation Facility using a VG DA30 electron analyzer under ultrahigh vacuum better than 5×10^{-11} Torr. The energy resolution is set to ∼12 meV for the band structure and ∼16 meV for Fermi surface mapping, while the angular resolution is set to 0.2°. Spectra are recorded at 30 K except if otherwise indicated. Growth procedures of samples for *in situ* STM/STS measurements are similar to those introduced above. STM measurements are carried out in ultrahigh-vacuum condition at 4.3 K with a home-made STM-MBE combined system. W tips are carefully calibrated on a Ag island before measurements. The tunneling conductance spectra are obtained using standard lock-in amplifier techniques with a root-mean-square oscillation voltage of 3 meV and a lock-in frequency of 791.1 Hz.

Density functional theory calculations employ the projector augmented wave (PAW) method encoded in the Vienna *Ab initio* Simulation Package (VASP) [30–32]. The PAW method is used to describe the wave functions near the core and the generalized gradient approximation within the Perdew-Burke-Ernzerhof parametrization is employed as the electron exchange-correlation functional [33]. For band-structure calculations, the cutoff energy of 500 eV is taken for expanding the wave functions into plane-wave basis. In the calculations, the Brillouin zone is sampled in the $\boldsymbol{k}$ space within the Monkhorst-Pack scheme [34]. The spin-orbit coupling is taken into account by the second variation method. For two-dimensional freestanding FeSe monolayer, the numbers of these $\boldsymbol{k}$ points are 11×11. In the edge-state calculations, a 24-Å vacuum layer is adopted and there are 59 Fe atoms and 59 Se atoms for the [100] edge and 60 Fe atoms and 62 Se atoms for the [110] edge.

III. RESULTS AND DISCUSSION

A. Sample characterization and local-density approximation results of band inversion

The crystal structure of monolayer $FeTe_{1-x}Se_x$/STO is presented in Fig. 1(a). The unit cell of monolayer $FeTe_{1-x}Se_x$/STO is tetragonal and contains two iron atoms. The sample quality is monitored by reflection high-energy electron diffraction (RHEED) during growth, as shown in Fig. 1(b). The exact Se content x of our sample is determined by *in situ* x-ray photoelectron spectroscopy (XPS) method. The results are shown in Fig. 1(c), where the value of $[x/(1-x)]$ of different samples is proportional to the ratio of the characteristic peak area weighted by atomic cross section of Se $3d$ and Te $4d$ orbitals, respectively. The main effect of the isovalent substitution of Te by Se is increasing the height of Se/Te surface H, which is labeled in Fig. 1(a). In addition, this substitution can enhance the spin-orbit coupling (SOC) splitting for d-orbital bands due to the intrinsic p-d hybridization. The Fermi surface of monolayer $FeTe_{1-x}Se_x$/STO ($x = 0.19$) is shown in Fig. 1(d). There are electron pockets at the M point, which have been observed in all superconducting monolayer $FeTe_{1-x}Se_x$/STO samples. They are believed to play an important role in promoting high-T_c superconductivity in this system [28].

Our local-density approximation (LDA) calculations reveal that a band inversion can be induced around the Γ point of freestanding monolayer FeSe with varying anion height. Note that freestanding monolayer films lack electron transfer from substrates compared with samples grown on STO [35,36] and the strong correlation effect in Fe(Te,Se). To directly compare with experiments, the calculated Fermi level is shifted to the value measured by ARPES. Strain effects from the substrate STO are modeled by setting the in-plane lattice constant of monolayers to be that of STO 3.905 Å. Figure 1(e) depicts the band structure with a low anion height before band inversion. Around the Γ point, there are three holelike bands (α, β, γ) and one electronlike band (η). With increasing H, the hybridization between Fe d_{xy} and Se p_z weakens and the η band starts to sink. As the η band and the α, β, γ bands have opposite inversion-symmetry eigenvalues, a band inversion between them will drive the system into a topologically nontrivial phase. As shown in Fig. 1(f) for $H = 1.54$ Å, the orbital character change of the η-band bottom from p_z/d_{xy} to d_{yz}/d_{xz} clearly demonstrates this band inversion. Simultaneously, the α-band top changes from d_{xz} to p_z/d_{xy} and this induces a parity change from even to odd with respect to the xz plane, which is direct evidence for the band inversion that can be verified by ARPES experiments.

B. Orbital analysis of band structure near topological critical point

In ARPES measurements, orbital and parity characters of bands can be determined by changing the photon energy and the polarization according to the matrix element effect [37,38]. We demonstrate the observation of two holelike bands (α, β) and one electronlike band (η) around the Γ point of monolayer $FeTe_{1-x}Se_x$ ($x = 0.21$) in Fig. 2 using photons with different energies and polarizations. The third

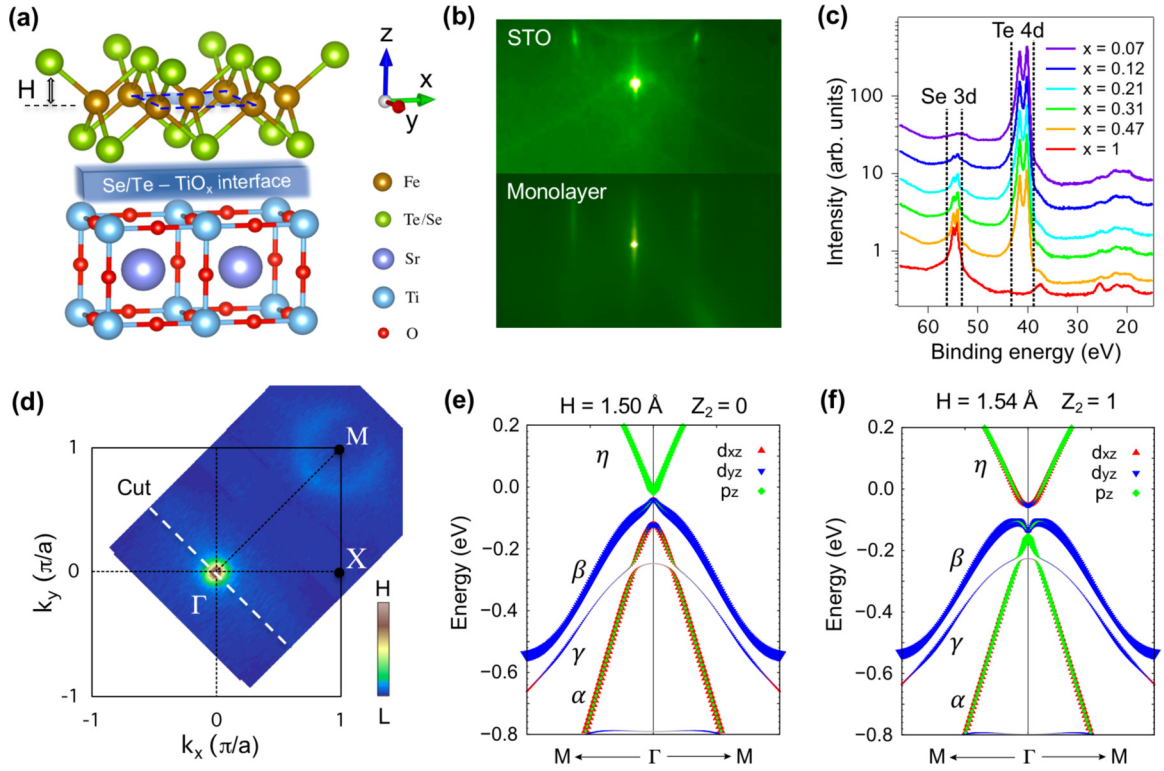

FIG. 1. (a) Schematic crystal structure of monolayer $FeTe_{1-x}Se_x$/STO. H is defined as the Te/Se height relative to the Fe plane. (b) Typical RHEED pattern of STO substrate (upper panel) after treatment in vacuum and $FeTe_{1-x}Se_x$/STO monolayer (lower panel) after annealing. (c) *In situ* XPS results of six samples with different Se content x detected by 100-eV photons. (d) Definition of the Brillouin zone of the two Fe unit cell. The Fermi surface of monolayer $FeTe_{0.81}Se_{0.19}$/STO is measured at $T = 15$ K. The intensity has been integrated in the ±10-meV energy range. White dashed line represents the cut position of ARPES spectrum shown in this paper. (e), (f) LDA calculation results of band structure for freestanding monolayer FeSe/STO with Se height $H = 1.50$ Å and $H = 1.54$ Å, respectively. Three holelike bands (α, β, γ) and one electronlike band η are predicted around Γ. The omitted orbital of the γ band is d_{xy} according to our calculations displayed in Appendix A.

γ band with dominant d_{xy} orbital component can hardly be observed because the spectral weight of d_{xy} is the smallest due to the strongest correlation among all the orbitals in iron-based superconductors [39]. The corresponding LDA results of d_{xy} orbital component are presented in Appendix A. Using our experimental facility, as shown in Fig. 2(a), odd (even) orbital with respect to the M_x mirror plane can be observed with p- (s-) polarized photons. The d_{yz} orbital is odd while d_{xz} is even. Moreover, the p_z orbital can be observed using p-polarized photons, which also contain the z component of photon polarization (vector potential A_z) in our facility geometry. The results of the matrix element effect analysis are summarized in Table I. Furthermore, to distinguish p and d orbitals, we can take advantage of the photoemission cross-section difference of Fe $3d$ and Te $5p$ (Se $4p$) in the energy range from 15 to 40 eV [40], as shown in Fig. 2(b).

Figures 2(c)–2(d) display ARPES results and the corresponding second derivative spectrum measured with p-polarized, 22-eV photons. The α and η bands can be observed clearly. These two bands form a Dirac-cone-like band structure, indicating that the system is close to the topological transition critical point. The energy of the Dirac point (DP) can be estimated in the momentum distribution curves (MDC) plot, as shown in Fig. 2(i). When the photon energy increases to 32 eV, as shown in Figs. 2(e) and 2(f), the spectral weight of the α and η bands is obviously suppressed, indicating the p_z orbital character of these bands. The residual weak spectral weight of the η band is attributed to its d_{xy} orbital character according to our LDA analysis presented in Appendix A. On the other hand, the β band becomes more apparent, suggesting its d_{yz} orbital character with odd parity. In Figs. 2(g) and 2(h), when we change the polarization geometry from p to s, only the α band can be detected, confirming its d_{xz} orbital character with even parity. By fitting the experimental bands to $E = C_0 + C_1|k| + C_2k^2$, we determine that the band tops of the α and β bands are located at 21.7 ± 0.5 meV and 25.7 ± 1.2 meV below E_F, respectively, and that the band bottom of the η band is at 20.3 ± 1.2 meV below E_F. We summarize the results of the band structure and orbital analysis of the $x = 0.21$ sample in Fig. 2(j).

To further verify the effect of cross section on the spectral weight variation presented in Figs. 2(c) and 2(e), we take more detailed photon energy dependent measurements as shown in Fig. 3. In Fig. 3(a), we could observe the gradual evolution of the spectral weight of α and β bands measured by p-polarized photons with energy range from 28 to 36 eV. On the contrary, results of s-polarized photons do not show such a phenomenon in Fig. 3(b) due to the lack of ability to detect the p_z orbital under such experimental geometry. We make quantitative MDC analyses for the data in Fig. 3(a) and display the corresponding

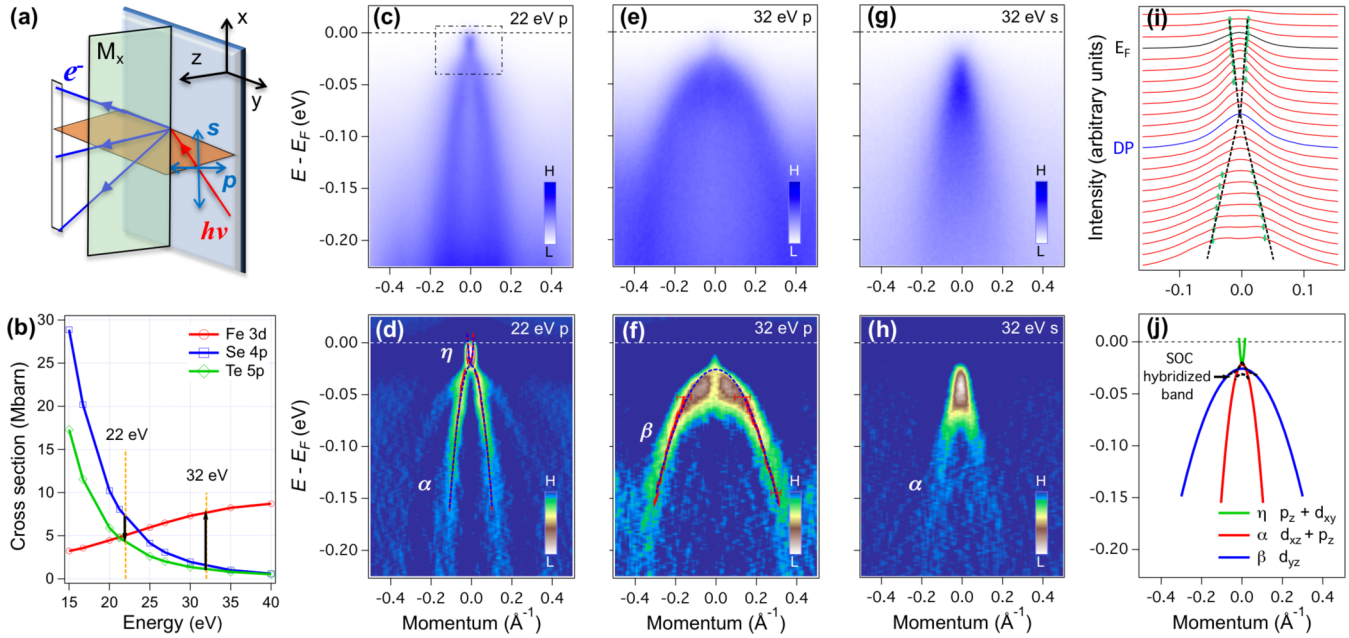

FIG. 2. Electronic structure near topological critical point ($x = 0.21$) around the Brillouin-zone center (Γ). (a) Schematic experimental geometry of ARPES measurements. (b) Comparison of cross section of Fe $3d$ and Se $4p$ (Te $5p$) [40]. (c), (d) Electronic structure around the Γ point detected by 22-eV p-polarized photons and the corresponding second derivative spectrum. Red dots in (d) represent peak position of MDC fitted by Lorentz function. Blue dashed curves are fitting results of the MDC peak position, using the function $E = C_0 + C_1|k| + C_2k^2$. (e)–(h) Same as (c), (d) but measured with (e), (f) 32-eV p-polarized photons and (g), (h) 32-eV s-polarized photons, respectively. (i) MDC plot of the dashed rectangular region in (c). Green dots show MDC peak position fitted by Lorentz function. Black dashed lines are schematic of the Dirac-cone-like dispersion after tracing the position of MDC peaks. The MDCs at energies of the Fermi level (E_F) and the DP are highlighted by black and blue, respectively. (j) Summary of the band structure and orbital analysis around Γ. The three solid curves are results of fitting of MDC peaks of the α, β, and η bands. Black dashed curves are the schematic results of band hybridization due to SOC.

MDC fitting results and the extraction method of the spectral weight in Appendix B. The extracted spectral weight of α and β bands are presented in Fig. 3(c) along with the calculated cross section [40] normalized by the orbital-dependent factor. The consistent evolution with photon energy in Fig. 3(c) confirms the rationality of cross-section interpretation and the existence of p_z orbital component in the Dirac-cone-like band structure.

C. Topological transition in monolayer $FeTe_{1-x}Se_x$/STO

If there is a topological transition in monolayer $FeTe_{1-x}Se_x$, as predicted in the aforementioned LDA calculations, the orbital and parity characters of the α, β, and η bands should exhibit a dramatic change through it. Moreover, as shown above, the sample with Se content $x = 0.21$ is already close to the critical point. To visualize the band-inversion process, we systematically study the band-structure evolution of monolayer $FeTe_{1-x}Se_x$ as a function of the Se content x.

TABLE I. ARPES matrix element effect of orbitals relevant to the band-inversion process. ✓ indicates that the orbital can be observed using the corresponding polarized photons, while × means that it cannot be observed. $k \neq 0$ indicates that the orbital can be observed away from the Γ point.

Pol.	d_{xz}	d_{yz}	p_z	d_{xy}
$\boldsymbol{s}(A_x)$	✓	×	$k \neq 0$	×
$\boldsymbol{p}(A_y)$	×	✓	×	$k \neq 0$
$\boldsymbol{p}(A_z)$	$k \neq 0$	×	✓	×

Figures 4(a)–4(c) show the band structures of six different Se content samples detected by 22-eV p-, 32-eV p-, and 32-eV s-polarized photons. With one particular photon energy, we can observe dramatic changes of bands in samples with different content. In Fig. 4(a), the spectral weight of the α band increases dramatically with decreasing Se content, indicating the increase of p_z orbital character in the α band. Moreover, as indicated by a red arrow in Fig. 4(a), the α-band top cannot be observed before the band inversion ($x > 0.21$). As the orbital character of the α-band top changes to p_z/d_{xy} during the band-inversion process, the α-band top becomes significantly enhanced after band inversion ($x < 0.21$). The enhancement of the α band can also be found in Fig. 4(b), which shows the evolution of d-orbital bands with odd parities. The β band is expected to be clear and the α band to be completely suppressed before the band inversion due to its even parity nature. However, the missing spectral weight indicated by a red arrow becomes apparent after the band inversion. Compared with Fig. 4(a), the reemerging band is attributed to the α band, which clearly suggests that the parity of the α-band top changes from even to odd. In contrast to results of p-polarized photons, the evolution of the α band exhibits the opposite behavior when measurements are performed with 32-eV s-polarized photons and only orbitals with even parities can be detected, as shown in Fig. 4(c). The

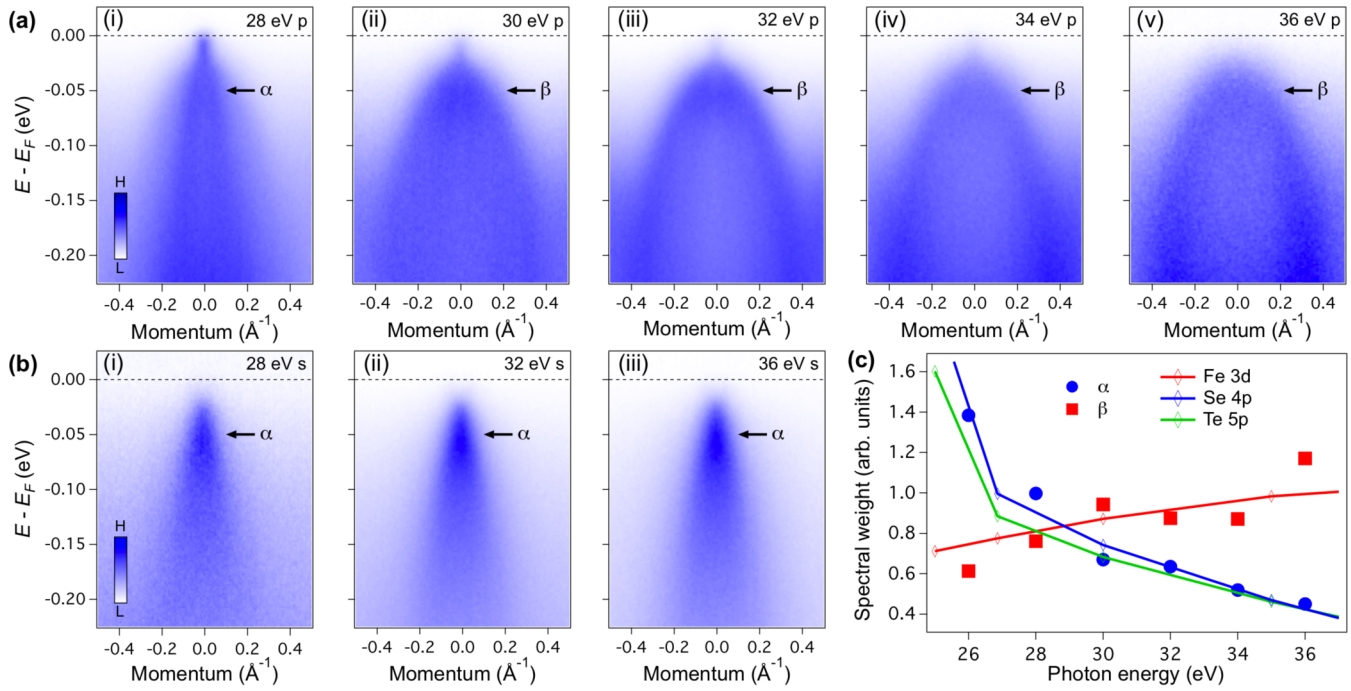

FIG. 3. (a) Band structure near topological critical point ($x = 0.21$) around the Brillouin-zone center (Γ) observed by (i) 28-, (ii) 30-, (iii) 32-, (iv) 34-, and (v) 36-eV p-polarized photons, respectively. The inner holelike band (α) and outer holelike band (β) are indicated by black arrows. (b) Same as (a) but measured by (i) 28-, (ii) 32-, and (iii) 36-eV s-polarized photons, respectively. (c) The extracted spectral weight evolution with photon energy along with the calculated cross section [40] normalized by the orbital-dependent factor. The blue circle and red square represent the spectral weight of α and β bands. The calculated cross-section values of Fe $3d$ (red), Se $4p$ (blue), and Te $5p$ (green) orbitals are divided by 8.381, 4.162, and 2.97, respectively, to correspond to the spectral weight value. The Lorentzian function fitting results of MDCs and the extraction method of the spectral weight are displayed in Appendix B.

spectral weight of the α-band top is clear before the band inversion, indicated by a green arrow, and is suppressed after the band inversion, which is also consistent with the above analysis.

We can also trace the evolution of the β band. In contrast to the α band, no obvious change occurs for the β band, except for a band shift to a lower binding energy. To see it more clearly, we show the MDC plot of the α and β bands in Figs. 4(d) and 4(e), respectively. The peak position of the α band continuously evolves toward the Γ point, while that of the β band is almost unchanged with the Se content decreasing. Then, we calculate the effective mass of the α, β, and η bands. The results are shown in Fig. 4(f). The effective mass of the three bands exhibits rather different trends with the variation of the Se content. When the Se content decreases, the value of the α band decreases dramatically while that of the η band increases rapidly. However, the effective mass of the β band remains almost unchanged. These changes of effective masses can be interpreted in terms of the orbital character change due to band inversion. Because the d orbitals exhibit stronger correlation effect than the p orbitals, the η band becomes more correlated due to the increasing d-orbital components, while the α band behaves oppositely due to the increasing p-orbital component, and the β band shows nearly no change, in agreement with its relative d and p components remaining the same in the process of band inversion.

D. Edge states in monolayer FeTe/STO

According to the bulk-boundary correspondence, topological edge states will appear at the edge of nontrivial monolayer $FeTe_{1-x}Se_x$/STO films [1]. We carry out LDA calculations for Fe-Te [100] and Fe-Fe [110] edges of monolayer FeTe, as shown in Figs. 5(a) and 5(d). The obtained band structures and local density of states (LDOS) for bulk and edge atoms are displayed in Figs. 5(b) and 5(c) for the [100] edge and Figs. 5(e) and 5(f) for the [110] edge. The nontrivial gap is located near E_F and gapless Dirac-cone-like edge states should appear in the region. Actually, this is the case for the (100) surface, as shown in Fig. 5(b). The edge states extend over nearly the whole Brillouin zone and merge into the bulk states near the M point. Due to the 1D nature of the Dirac band dispersion, the edge LDOS is almost a constant near the nontrivial gap. With decreasing energy, the edge LDOS increases rapidly and develops a peak below the gap, which is attributed to the flat dispersion of edge states. A similar peak can also be found in the LDOS of the [110] edge, although a constant LDOS nearly disappears due to the strong overlap between the edge and bulk states, as shown in Figs. 5(e) and 5(f).

To demonstrate the edge states experimentally, *in situ* STM/STS measurements are carried out after growth of monolayer FeTe/STO. Topographic images of monolayer FeTe containing Fe-Te [100] and Fe-Fe [110] edges are presented in Figs. 5(g) and 5(h), respectively. The insets of

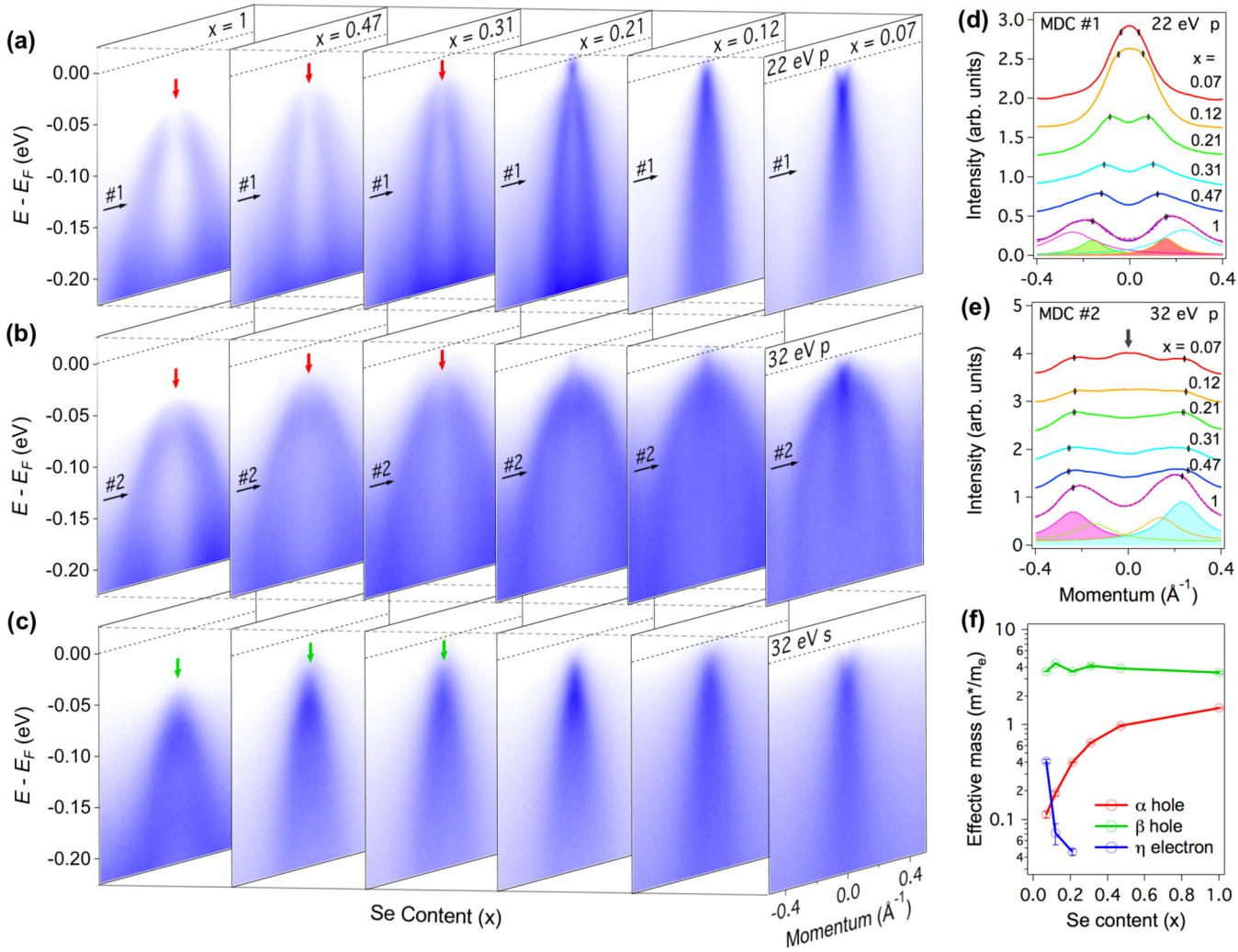

FIG. 4. Band inversion in monolayer $FeTe_{1-x}Se_x$/STO. (a)–(c) Electronic structure evolution with Se content, detected by (a) 22-eV *p*-polarized, (b) 32-eV *p*-polarized and (c) 32-eV *s*-polarized photons, respectively. The Se contents x of six samples (from left to right) are 1, 0.47, 0.31, 0.21, 0.12, and 0.07, which are determined by *in situ* XPS method. The red arrows in (a) and (b) show the relatively weak intensity around Γ before the topological transition. The green arrows in (c) indicate the appearance of band top. (d), (e) MDC plot of six samples at energy positions pointed by No. 1 in (a) and No. 2 in (b), respectively. Position of No. 1 and No. 2 is 80 meV below the α- and β-band tops. Four Lorentzian-function fitting results for the $x = 1$ sample are presented at the bottom of (d) and (e). Black dots on each MDC are fitting results of the peak positions. Lorentzian function curves associated with the α and β bands are shaded in (d) and (e), respectively. The black arrow in (e) indicates the appearance of the α band after the topological transition. (f) Effective mass evolution with Se content. The values of the α, β, and η bands are shown by red, green, and blue, respectively.

Figs. 5(g) and 5(h) show the atomically resolved topography indicating the high quality of our sample. We take STS measurements along the lines indicated by the yellow arrows in Figs. 5(g) and 5(h) from the edges of the Fe-Te and Fe-Fe directions to the inside film, as shown in Figs. 5(i) and 5(j). The common feature is that noticeable enhancements around 50 meV below E_F (30 meV below the η-band bottom) appear for the edges compared with the bulk, which decay to the bulk value within several nanometers. According to the calculated results in Fig. 5(b), we find that the edge states connecting the η band at the Γ point and the electron δ band at the M point have a section of flat dispersion around the band bottom of the δ band, which probably corresponds to the enhanced DOS. Although the exact value of the calculated binding energy is not reliable due to strong correlations in FeTe, the band bottom of the δ band is reported experimentally to reside around 50 meV below E_F [28], which is consistent with the energy observed in STM/STS measurements. Therefore, the increased DOS around this energy level is qualitatively consistent with our LDA calculations. Furthermore, for the spectra of the Fe-Te edge, a plateau of DOS appears around 0 to 20 meV below E_F in Fig. 5(i), which probably corresponds to the 1D Dirac cone of the nontrivial edge states, consistent with our LDA calculations in Fig. 5(b) and 5(c). The energy value of the Dirac point matches well with the band-structure results shown in Fig. 2(c).

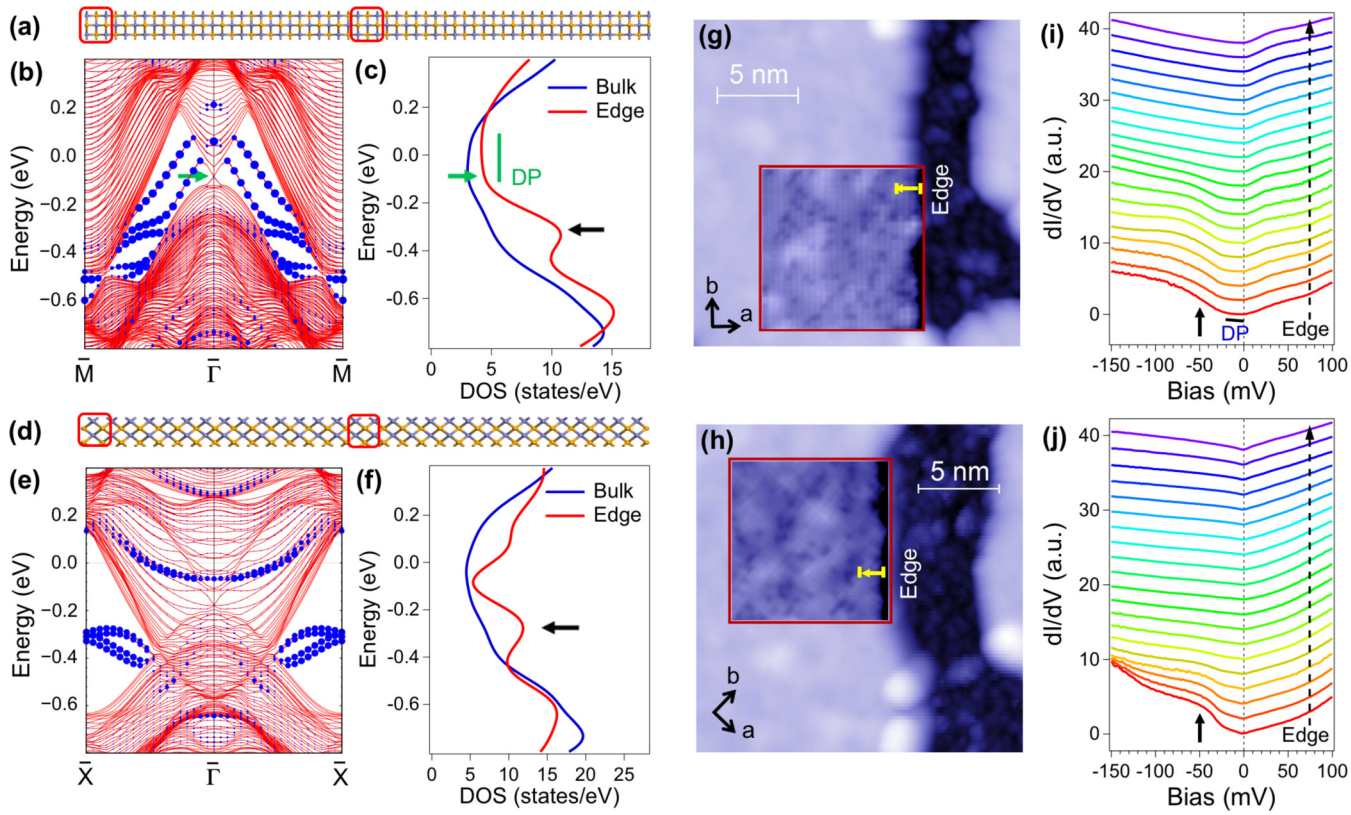

FIG. 5. Edge states in monolayer FeTe/STO. (a) Model of atomic chain along the Fe-Te direction. (b) One-dimensional band structure for the atomic chain in (a). The green arrow represents the position of the Dirac point and the sizes of the blue circles represent the contributions of the left edge. (c) Calculated LDOS of bulk and edge for model (a). The black arrow corresponds to the LDOS enhancement mainly due to the flat dispersion of edge states. (d)–(f) Same as (a)–(c) but for the atomic chain along the Fe-Fe direction. (g), (h) Experimental STM topography of the Fe-Te edge ($V = 500$ mV, $I = 50$ pA) and the Fe-Fe edge ($V = 1$ V, $I = 50$ pA) of FeTe/STO monolayer. Notice that the roughness of the film is mainly due to STO substrate instead of Te/Se height difference as shown in Appendix C. The inset shows the atomically resolved topography with the edge along Fe-Te ($V = 100$ mV, $I = 0.5$ nA) and Fe-Fe direction ($V = 100$ mV, $I = 1$ nA), respectively. (i), (j) *dI/dV* spectra (junction setpoint $V = 100$ mV, $I = 0.2$ nA) from edge to bulk detected along the yellow arrow shown in (g) and (h), respectively. The black arrows show the DOS enhancement near the edge. The plateau labeled DP in (i) indicates the existence of Dirac point.

IV. CONCLUSIONS

Our ARPES and LDA calculation results provide direct evidence of topological transition in high-T_c $FeTe_{1-x}Se_x$/STO monolayers. These observations are vital to confirm the mechanism of band inversion in this system. Many theoretical works propose that chalcogenide anions play an important role in determining topological properties, where the hybridization between chalcogenide anions and iron cations tuned by the Se/Te plane height leads to the band inversion between electronlike bands with p_z/d_{xy}-orbital and holelike bands with d_{xz}/d_{yz} orbital [8,14,15,29]. It is quite distinct from the magnetism scenario in monolayer FeSe [26]. In our experiments, we directly observe the electron band with p_z/d_{xy} orbital character for samples with Se content $x \leqslant 0.21$ and its systematic effective mass evolution during the band-inversion process, supporting the crucial role of chalcogenide anions in the realization of band inversion in $FeTe_{1-x}Se_x$/STO monolayers.

The consistency of STM/STS experiments and ARPES/LDA results provides evidence for the existence of edge states, even for the 1D Dirac cone. Due to the complexity of the metallic bulk states influencing the detection of edges states in the experiment, the evidence in STM experiment is highly suggestive but not conclusive for the topological origin of the edge states. The further confirmation of topological nontrivial character of edge states leaves room for further exploration, such as backscattering experiments [41]. In contrast to bulk materials, the direct observation of edge states in $FeTe_{1-x}Se_x$ monolayers is extremely challenging in ARPES experiments. We propose that these states could be observed by performing ARPES measurements of $FeTe_{1-x}Se_x$ monolayers grown on high miscut STO substrates with densely parallel edges, which is left as future work.

$FeTe_{1-x}Se_x$/STO monolayers are promising to search for Majorana bound states due to the integration of topological nontrivial character and high-T_c superconductivity [27,28] in one material. The Dirac cone of edge states lies close to the Fermi level from STM measurements. Moreover, the position of topological bands can be tuned by abundant methods for this system, including post-anneal treatment [18], alkali

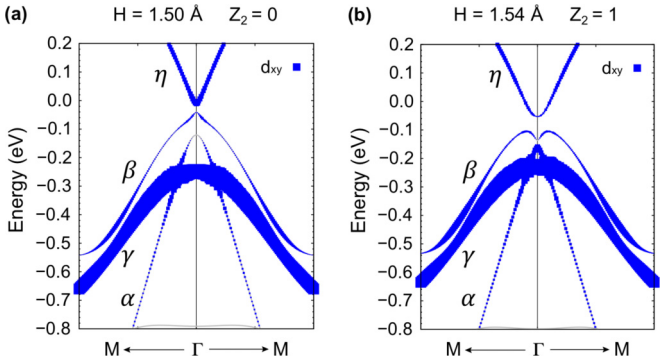

FIG. 6. LDA calculation results of d_{xy} orbital component of bands around the Γ point for freestanding monolayer FeSe/STO with Se height (a) $H = 1.50$ Å and (b) $H = 1.54$ Å, respectively. The size of the pink circles represents the proportion of d_{xy} orbital.

metal doping [42,43], changing various substrates [44–46], and electric-field regulation [47–49]. Compared with its bulk counterpart, monolayer $FeTe_{1-x}Se_x$/STO system is more compatible with devices through micro/nanoprocessing technology and could be easier to regulate. When the topological edge states are tuned to the Fermi level, superconducting topological states can be induced through the bulk proximity effect. If a magnetic thin film is further deposited on parts of superconducting edges to suppress superconductivity, Majorana bound states are expected to appear at the domain wall between the superconducting and magnetic insulating regions. Due to the high superconducting transition temperature in $FeTe_{1-x}Se_x$/STO monolayers and their two-dimensional nature, our discovery of their topological nontrivial properties provides us a simple and tunable platform for realizing and manipulating Majorana bound states at high temperature.

ACKNOWLEDGMENTS

We thank P. Zhang, Z.-Q. Han, and L.-Y. Kong for useful discussions. This work is supported by grants from the Chinese Academy of Sciences (Grants No. XDB28000000 and XDB07000000), the Ministry of Science and Technology of China (Grants No. 2016YFA0401000, No. 2015CB921000, No. 2016YFA0300600, No. 2016YFA0302400, and No. 2016YFA0300600), and the National Natural Science Foundation of China (Grants No. 11574371, No. 11622435, No. U1832202, and No. 11888101). Y.-B.H. acknowledges support by the CAS Pioneer "Hundred Talents Program" (type C). P.R. acknowledges the funding from the Canada First Research Excellence Fund.

X-L.P, Y.L, and X.-X.W contributed equally to this work; H.D., Y.-J.S. and H.-Q.M. supervised the project; X.-L.P., Y.L., H.-B.D., H.-Q.M., and Y.-J.S. synthesized the samples; X.-L.P. performed the ARPES measurements with help from

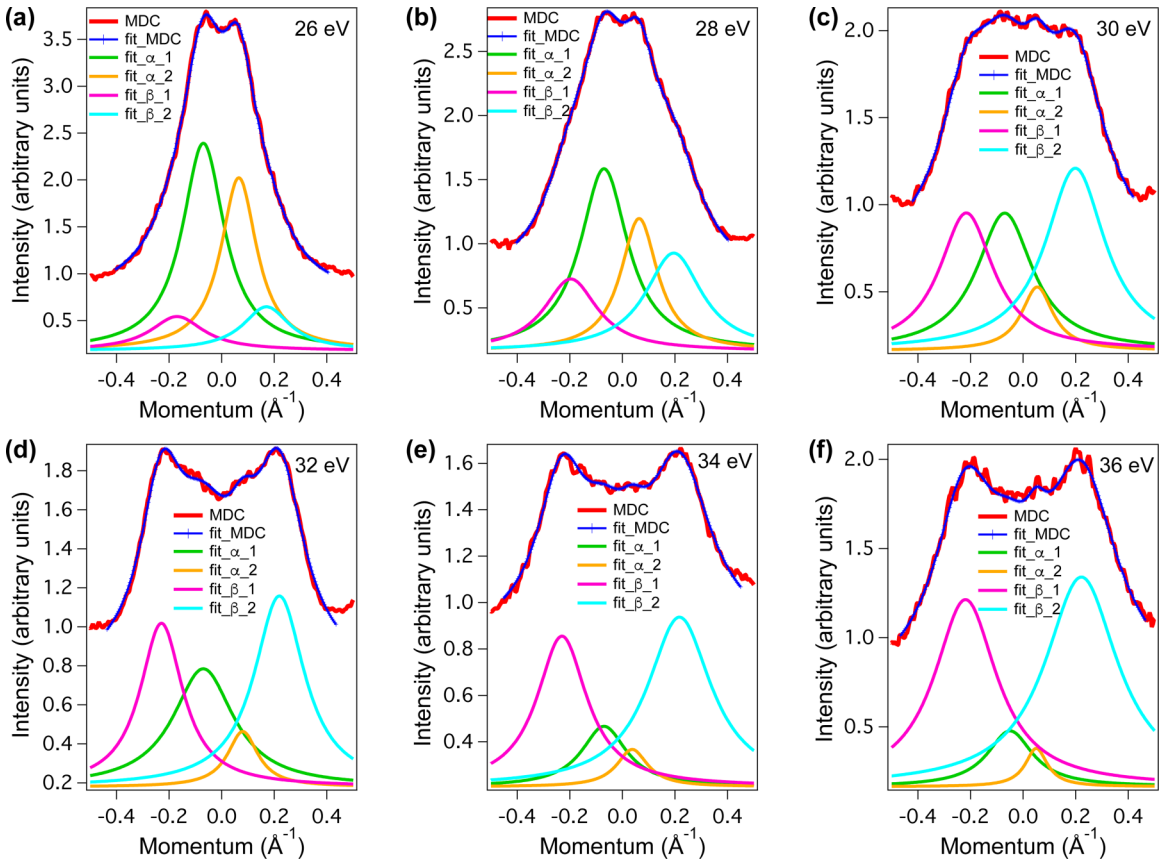

FIG. 7. Lorentzian-function fitting results of MDC at $E–E_F = -0.1$ eV extracted from the data shown in Fig. 3(a) which are observed by (a) 26-, (b) 28-, (c) 30-, (d) 32-, (e) 34, and (f) 36-eV *p*-polarized photons, respectively.

X.S., W.-H.F., M.L., and Y.-B.H.; X-.L.P., Y.-J.S., and H.D. analyzed the ARPES data; Y.L., H.-B.D., and H.-Q.M. performed the STM/STS measurements and analyzed the data with input from S.-H.P.; X.-X.W., and J.-P.H. performed the LDA calculations and provided theoretical input; X.-L.P., X.-X.W., P.R., Y.L., H.-Q.M., Y.-J.S., and H.D. wrote the manuscript. All authors discussed the results and commented on the manuscript.

APPENDIX A: LDA RESULTS OF d_{xy} ORBITAL COMPONENT AROUND Γ POINT

Our LDA calculations reveal the d_{xy} orbital distribution during the band-inversion process around the Γ point of freestanding monolayer FeSe with varying anion height H. The definition of H is shown in Fig. 1(a). The γ band is mainly composed of d_{xy} orbital as shown in Fig. 6. Besides, the η band has a d_{xy} component before band inversion as presented in Fig. 6(a). With increasing H, the hybridization between Fe d_{xy} and Se p_z weakens and the η band starts to sink. As the η band and the α, β, and γ bands have opposite inversion-symmetry eigenvalues, band inversion between them will drive the system into a topologically nontrivial phase. After band inversion, the d_{xy}-orbital component increases in the band top of the α band, as shown in Fig. 6(b).

APPENDIX B: QUANTITATIVE ANALYSES OF THE SPECTRA WEIGHT

To justify the effect of cross section on the spectral weight evolution with photon energy, the quantitative analysis has been tried. We extracted the momentum distribution curve at $E–E_F = -0.1$ eV of data shown in Fig. 3(a) and then fitted these MDCs by four Lorentzian function. All MDCs are renormalized by their intensity at 0.5 $Å^{-1}$ where no bands cross. The corresponding results are shown in Fig. 7. Then we calculated the area of the fitting Lorentzian function of the α and β bands, respectively. Each area equals to the summation of the left part (fit function 1) and the right part (fit function 2). The spectral weight of these bands is proportional to their corresponding total area of the fitting functions.

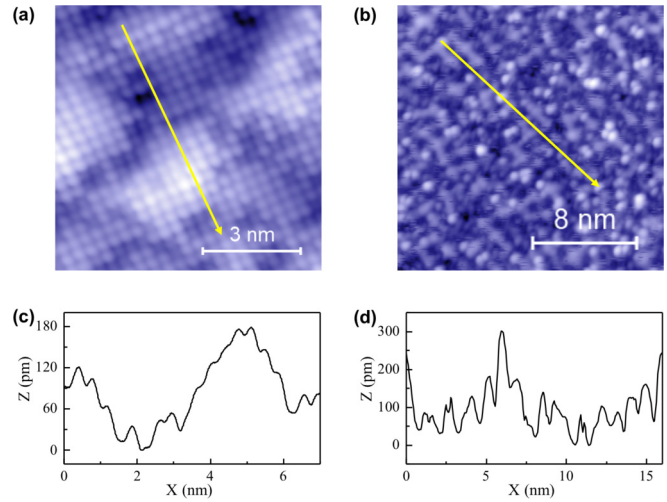

FIG. 8. Surface corrugation of monolayer $FeTe_{1-x}Se_x$ and STO substrate. (a), (b) STM topographic images of $FeTe_{1-x}Se_x$/STO(001) (100 mV,100 pA) and STO(001) substrate (1 V,10 pA), respectively. (c), (d) Line profile along the yellow line in (a), (b), respectively.

APPENDIX C: CORRUGATION OF THE SAMPLE SURFACE

The surface of monolayer $FeTe_{1-x}Se_x$/STO is rough, which is characterized by the topographic image with atoms of different brightness (indicating various height), as shown in Fig. 8(a). The surface corrugation or the height difference between the atoms is approximately 180 pm, as shown in Fig. 8(c). The height difference of monolayer $FeTe_{1-x}Se_x$ is larger than that of a thick film or a single crystal. In the latter, the atoms only show two kinds of brightness (height) while the bright atom is Te atom and the dark one is Se atom [50]. In monolayer $FeTe_{1-x}Se_x$, however, there are brighter and darker atoms, and the brighter atom cannot simply be assigned to Te and the darker to Se. As a consequence, statistical analysis of the image is not appropriate to gain the Te/Se ratio. The large corrugation is probably due to the roughness of the substrate, which shows no atomic flat surface, as presented in Figs. 8(b) and 8(d).

[1] X. L. Qi and S. C. Zhang, Topological insulators and superconductors, Rev. Mod. Phys., **83**, 1057 (2011).
[2] S. R. Elliott and M. Franz, Colloquium: Majorana fermions in nuclear, particle, and solid-state physics, Rev. Mod. Phys. **87**, 137 (2015).
[3] C. Kallin, Chiral p-wave order in Sr_2RuO_4, Rep. Prog. Phys. **75**, 042501 (2012).
[4] A. P. Mackenzie and Y. Maeno, The superconductivity of Sr_2RuO_4 and the physics of spin-triplet pairing, Rev. Mod. Phys. **75**, 657 (2003).
[5] L. Fu and C. L. Kane, Superconducting Proximity Effect and Majorana Fermions at the Surface of a Topological Insulator, Phys. Rev. Lett. **100**, 096407 (2008).
[6] H.-H. Sun, K.-W. Zhang, L.-H. Hu, C. Li, G.-Y. Wang, H.-Y. Ma, Z.-A. Xu, C.-L. Gao, D.-D. Guan, and Y.-Y. Li *et al.*, Majorana Zero Mode Detected with Spin Selective Andreev Reflection in the Vortex of a Topological Superconductor, Phys. Rev. Lett. **116**, 257003 (2016).
[7] N. Hao and J. Hu, Topological quantum states of matter in iron-based superconductors: from concept to material realization, Natl. Sci. Rev. **6**, 213 (2018).
[8] Z. Wang, P. Zhang, G. Xu, L. K. Zeng, H. Miao, X. Xu, T. Qian, H. Weng, P. Richard, and A. V. Fedorov *et al.*, Topological nature of the $FeSe_{0.5}Te_{0.5}$ superconductor, Phys. Rev. B **92**, 115119 (2015).
[9] G. Xu, B. Lian, P. Z. Tang, X. L. Qi, and S. C. Zhang, Topological Superconductivity on the Surface of Fe-Based Superconductors, Phys. Rev. Lett. **117**, 047001 (2016).
[10] P. Zhang, K. Yaji, T. Hashimoto, Y. Ota, T. Kondo, K. Okazaki, Z. J. Wang, J. S. Wen, G. D. Gu, and H. Ding *et al.*, Observation of topological superconductivity on the surface of an iron-based superconductor, Science **360**, 182 (2018).

[11] D. F. Wang, L. Y. Kong, P. Fan, H. Chen, S. Y. Zhu, W. Y. Liu, L. Cao, Y. J. Sun, S. X. Du, and J. Schneeloch *et al.*, Evidence for Majorana bound states in an iron-based superconductor, Science **362**, 333 (2018).

[12] Y. F. Lv, W. L. Wang, Y. M. Zhang, H. Ding, W. Li, L. L. Wang, K. He, C. L. Song, X. C. Ma, and Q. K. Xue, Experimental signature of topological superconductivity and Majorana zero modes on β-Bi_2Pd thin films, Sci. Bull. **62**, 852 (2017).

[13] X. Wu, S. Qin, Y. Liang, C. Le, H. Fan, and J. Hu, CaFeAs: A staggered intercalation of quantum spin Hall and high-temperature superconductivity, Phys. Rev. B **91**, 081111(R) (2015).

[14] P. Zhang, Z. J. Wang, X. X. Wu, K. Yaji, Y. Ishida, Y. Kohama, G. Y. Dai, Y. Sun, C. Bareille, and K. Kuroda *et al.*, Multiple topological states in iron-based superconductors, Nat. Phys. **15**, 41 (2019).

[15] Q. Liu, C. Chen, T. Zhang, R. Peng, Y.-J. Yan, C.-H.-P. Wen, X. Lou, Y.-L. Huang, J.-P. Tian, and X.-L. Dong *et al.*, Robust and Clean Majorana Zero Mode in the Vortex Core of High-Temperature Superconductor $(Li_{0.84}Fe_{0.16})$OHFeSe, Phys. Rev. X **8**, 041056 (2018).

[16] Q. Y. Wang, Z. Li, W. H. Zhang, Z. C. Zhang, J. S. Zhang, W. Li, H. Ding, Y. B. Ou, P. Deng, and K. Chang *et al.*, Interface-Induced High-Temperature Superconductivity in Single Unit-Cell FeSe Films on $SrTiO_3$, Chin. Phys. Lett. **29**, 037402 (2012).

[17] D. F. Liu, W. H. Zhang, D. X. Mou, J. F. He, Y. B. Ou, Q. Y. Wang, Z. Li, L. L. Wang, L. Zhao, and S. L. He *et al.*, Electronic origin of high-temperature superconductivity in single-layer FeSe superconductor, Nat. Commun. **3**, 931 (2012).

[18] S. L. He, J. F. He, W. H. Zhang, L. Zhao, D. F. Liu, X. Liu, D. X. Mou, Y. B. Ou, Q. Y. Wang, and Z. Li *et al.*, Phase diagram and electronic indication of high-temperature superconductivity at 65 K in single-layer FeSe films, Nat. Mater. **12**, 605 (2013).

[19] S. Y. Tan, Y. Zhang, M. Xia, Z. R. Ye, F. Chen, X. Xie, R. Peng, D. F. Xu, Q. Fan, and H. C. Xu *et al.*, Interface-induced superconductivity and strain-dependent spin density waves in FeSe/$SrTiO_3$ thin films, Nat. Mater. **12**, 634 (2013).

[20] J. J. Lee, F. T. Schmitt, R. G. Moore, S. Johnston, Y. T. Cui, W. Li, M. Yi, Z. K. Liu, M. Hashimoto, and Y. Zhang *et al.*, Interfacial mode coupling as the origin of the enhancement of Tc in FeSe films on $SrTiO_3$, Nature (London) **515**, 245 (2014).

[21] J. F. Ge, Z. L. Liu, C. H. Liu, C. L. Gao, D. Qian, Q. K. Xue, Y. Liu, and J. F. Jia, Superconductivity above 100 K in single-layer FeSe films on doped $SrTiO_3$, Nat. Mater. **14**, 285 (2015).

[22] Z. C. Zhang, Y. H. Wang, Q. Song, C. Liu, R. Peng, K. A. Moler, D. L. Feng, and Y. Y. Wang, Onset of the Meissner effect at 65 K in FeSe thin film grown on Nb-doped $SrTiO_3$ substrate, Sci. Bull. **60**, 1301 (2015).

[23] X. Shi, Z. Q. Han, X. L. Peng, P. Richard, T. Qian, X. X. Wu, M. W. Qiu, S. C. Wang, J. P. Hu, and Y. J. Sun *et al.*, Enhanced superconductivity accompanying a Lifshitz transition in electron-doped FeSe monolayer, Nat. Commun. **8**, 14988 (2017).

[24] N. N. Hao and J. P. Hu, Topological Phases in the Single-Layer FeSe, Phys. Rev. X **4**, 031053 (2014).

[25] N. N. Hao and S. Q. Shen, Topological superconducting states in monolayer FeSe/$SrTiO_3$, Phys. Rev. B, **92**, 165104 (2015).

[26] Z. F. Wang, H. M. Zhang, D. F. Liu, C. Liu, C. J. Tang, C. L. Song, Y. Zhong, J. P. Peng, F. S. Li, and C. N. Nie *et al.*, Topological edge states in a high-temperature superconductor FeSe/$SrTiO_3$(001) film, Nat. Mater. **15**, 968 (2016).

[27] F. Li, H. Ding, C. Tang, J. Peng, Q. Zhang, W. Zhang, G. Zhou, D. Zhang, C.-L. Song, and K. He *et al.*, Interface-enhanced high-temperature superconductivity in single-unit-cell $FeTe_{1-x}Se_x$ films on $SrTiO_3$, Phys. Rev. B **91**, 220503(R) (2015).

[28] X. Shi, Z. Q. Han, P. Richard, X. X. Wu, X. L. Peng, T. Qian, S. C. Wang, J. P. Hu, Y. J. Sun, and H. Ding, $FeTe_{1-x}Se_x$ monolayer films: Towards the realization of high-temperature connate topological superconductivity, Sci. Bull. **62**, 503 (2017).

[29] X. X. Wu, S. S. Qin, Y. Liang, H. Fan, and J. P. Hu, Topological characters in $Fe(Te_{1-x}Se_x)$ thin films, Phys. Rev. B **93**, 115129 (2016).

[30] G. Kresse and J. Hafner, Ab initio molecular-dynamics for liquid-metals, Phys. Rev. B **47**, 558 (1993).

[31] G. Kresse and J. Furthmuller, Efficiency of ab-initio total energy calculations for metals and semiconductors using a plane-wave basis set, Comput. Mater. Sci. **6**, 15 (1996).

[32] G. Kresse and J. Furthmuller, Efficient iterative schemes for ab initio total-energy calculations using a plane-wave basis set, Phys. Rev. B **54**, 11169 (1996).

[33] J. P. Perdew, K. Burke, and M. Ernzerhof, Generalized Gradient Approximation Made Simple, Phys. Rev. Lett. **77**, 3865 (1996).

[34] H. J. Monkhorst and J. D. Pack, Special points for Brillouin-Zone integrations, Phys. Rev. B **13**, 5188 (1976).

[35] H. M. Zhang, D. Zhang, X. W. Lu, C. Liu, G. Y. Zhou, X. C. Ma, L. L. Wang, P. Jiang, Q. K. Xue, and X. H. Bao, Origin of charge transfer and enhanced electron-phonon coupling in single unit-cell FeSe films on $SrTiO_3$, Nat. Commun. **8**, 214 (2017).

[36] W. W. Zhao, M. D. Li, C. Z. Chang, J. Jiang, L. J. Wu, C. X. Liu, J. S. Moodera, Y. M. Zhu, and M. H. W. Chan, Direct imaging of electron transfer and its influence on superconducting pairing at FeSe/$SrTiO_3$ interface, Sci. Adv. **4**, eaao2682 (2018).

[37] X.-P. Wang, P. Richard, Y.-B. Huang, H. Miao, L. Cevey, N. Xu, Y.-J. Sun, T. Qian, Y.-M. Xu, and M. Shi *et al.*, Orbital characters determined from Fermi surface intensity patterns using angle-resolved photoemission spectroscopy, Phys. Rev. B **85**, 214518 (2012).

[38] P. Richard, T. Qian, and H. Ding, ARPES measurements of the superconducting gap of Fe-based superconductors and their implications to the pairing mechanism, J. Phys.: Condens. Matter **27**, 293203 (2015).

[39] M. Yi, Y. Zhang, Z.-X. Shen, and D. Lu, Role of the orbital degree of freedom in iron-based superconductors, npj Quantum Mater. **2**, 57 (2017).

[40] J. J. Yeh and I. Lindau, Atomic subshell photoionization cross-sections and asymmetry parameters: $1 \leqslant Z \leqslant 103$, At. Data Nucl. Data Tables **32**, 1 (1985).

[41] I. K. Drozdov, A. Alexandradinata, S. Jeon, S. Nadj-Perge, H. W. Ji, R. J. Cava, B. A. Bernevig, and A. Yazdani, One-dimensional topological edge states of bismuth bilayers, Nat. Phys. **10**, 664 (2014).

[42] Y. Miyata, K. Nakayama, K. Sugawara, T. Sato, and T. Takahashi, High-temperature superconductivity in potassium-coated multilayer FeSe thin films, Nat. Mater. **14**, 775 (2015).

[43] G. N. Phan, K. Nakayama, S. Kanayama, M. Kuno, K. Sugawara, T. Sato, and T. Takahashi, High-temperature

superconductivity and lattice relaxation in lithium-deposited FeSe on $SrTiO_3$, J. Phys. Soc. Jpn. **86**, 033706 (2017).

[44] R. Peng, H. C. Xu, S. Y. Tan, H. Y. Cao, M. Xia, X. P. Shen, Z. C. Huang, C. H. P. Wen, Q. Song, and T. Zhang *et al.*, Tuning the band structure and superconductivity in single-layer FeSe by interface engineering, Nat. Commun. **5**, 5044 (2014).

[45] P. Zhang, X.-L. Peng, T. Qian, P. Richard, X. Shi, J.-Z. Ma, B. B. Fu, Y.-L. Guo, Z. Q. Han, and S. C. Wang *et al.*, Observation of high-T_c superconductivity in rectangular FeSe/$SrTiO_3$(110) monolayers, Phys. Rev. B **94**, 104510 (2016).

[46] S. N. Rebec, T. Jia, C. Zhang, M. Hashimoto, D. H. Lu, R. G. Moore, and Z. X. Shen, Coexistence of Replica Bands and Superconductivity in FeSe Monolayer Films, Phys. Rev. Lett. **118**, 067002 (2017).

[47] B. Lei, J. H. Cui, Z. J. Xiang, C. Shang, N. Z. Wang, G. J. Ye, X. G. Luo, T. Wu, Z. Sun, and X. H. Chen, Evolution of High-Temperature Superconductivity from a Low-T_c Phase Tuned by Carrier Concentration in FeSe Thin Flakes, Phys. Rev. Lett. **116**, 077002 (2016).

[48] J. Shiogai, Y. Ito, T. Mitsuhashi, T. Nojima, and A. Tsukazaki, Electric-field-induced superconductivity in electrochemically etched ultrathin FeSe films on $SrTiO_3$ and MgO, Nat. Phys. **12**, 42 (2016).

[49] K. Hanzawa, H. Sato, H. Hiramatsu, T. Kamiya, and H. Hosono, Electric field-induced superconducting transition of insulating FeSe thin film at 35 K, Proc. Natl. Acad. Sci. USA **113**, 3986 (2016).

[50] X. B. He, G. R. Li, J. D. Zhang, A. B. Karki, R. Y. Jin, B. C. Sales, A. S. Sefat, M. A. McGuire, D. Mandrus, and E. W. Plummer, Nanoscale chemical phase separation in $FeTe_{0.55}Se_{0.45}$ as seen via scanning tunneling spectroscopy, Phys. Rev. B **83**, 220502(R) (2011).